ACS NANO
Cite This: ACS Nano 2019, 13, 3896−3909
www.acsnano.org

ARTICLE

WS_2 Nanotubes, 2D Nanomeshes, and 2D In-Plane Films through One Single Chemical Vapor Deposition Route

Zichen Liu,[†,§,∥] Alexander William Allen Murphy,[‡,§,∥] Christian Kuppe,[‡,§,∥] David Charles Hooper,[‡,§,∥] Ventsislav Kolev Valev,[‡,§,∥] and Adelina Ilie*[,†,§,∥]

[†]Centre for Graphene Science, University of Bath, Bath BA2 7AY, United Kingdom
[‡]Centre for Photonics and Photonic Materials, University of Bath, Bath BA2 7AY, United Kingdom
[§]Centre for Nanoscience and Nanotechnology, University of Bath, Bath BA2 7AY, United Kingdom
[∥]Department of Physics, University of Bath, Claverton Down, Bath BA2 7AY, United Kingdom

Supporting Information

ABSTRACT: We demonstrate a versatile, catalyst free chemical vapor deposition process on insulating substrates capable of producing in one single stream one-dimensional (1D) WO_{3-x} suboxides leading to a wide range of substrate-supported 2H-WS_2 polymorphs: a tunable class of out-of-plane (of the substrate) nanophases, with 1D nanotubes and a pure WS_2, two-dimensional (2D) nanomesh (defined as a network of webbed, micron-size, few-layer 2D sheets) at its extremes; and in-plane (parallel to the substrate) mono- and few-layer 2D domains. This entails a two-stage approach in which the $2WO_3 + 7S \rightarrow 2WS_2 + 3SO_2$ reaction is intentionally decoupled. First, various morphologies of nanowires or nanorods of high stoichiometry, $WO_{2.92}/WO_{2.9}$ suboxides (belonging to the class of Magnéli phases) were formed, followed by their sulfurization to undergo reduction to the aforementioned WS_2 polymorphs. The continuous transition of WS_2 from nanotubes to the out-of-plane 2D nanomesh, *via* intermediary, mixed 1D-2D phases, delivers tunable functional properties, for example, linear and nonlinear optical properties, such as reflectivity (linked to optical excitations in the material), and second harmonic generation (SHG) and onset of saturable absorption. The SHG effect is very strong across the entire tunable class of WS_2 nanomaterials, weakest in nanotubes, and strongest in the 2D nanomesh. Furthermore, a mechanism *via* suboxide (WO_{3-x}) intermediate as a possible path to 2D domain growth is demonstrated. 2D, in-plane WS_2 domains grow *via* "self-seeding and feeding" where short $WO_{2.92}/WO_{2.9}$ nanorods provide both the nucleation sites and the precursor feedstock. Understanding the reaction path (here, in the W−O−S space) is an emerging approach toward controlling the nucleation, growth, and morphology of 2D domains and films of transition-metal dichalcogenides.

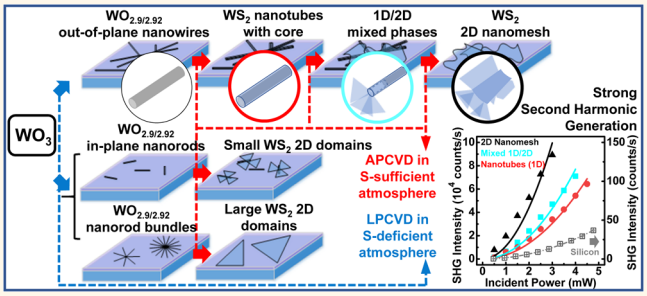

KEYWORDS: *WS_2 and WO_{3-x} suboxides, transition-metal dichalcogenides, two-dimensional layered materials, nanotubes, chemical vapor deposition growth, linear and nonlinear optical properties, second harmonic generation*

Two-dimensional (2D) transition-metal dichalcogenides (TMDs), the inorganic analogues of graphene, have attracted significant attention in recent years.[1−5] Chemical vapor deposition (CVD) has emerged as one of the most efficient and versatile methods for the large area synthesis of a wide range of 2D TMDs.[6−11] By varying deposition parameters and improving the CVD apparatus, larger and larger domain TMD mono- and few-layer films have been recently reported.[12,13]

Among the more than 40 varieties of TMDs,[14] WS_2 and WSe_2 have attracted significant attention due to their giant spin−orbit splitting, a property of particular interest for spintronics,[15] as well as optical materials.[16,17] In the case of WS_2, WO_3 and S powders are the precursors most widely used for growth by CVD.[18] WO_3 is converted into WS_2 by sulfurization with the proposed reaction being $2WO_3 + 7S \rightarrow 2WS_2 + 3SO_2$.[19] However, this conversion process is not trivial, as the W atom sites in the WO_3 monoclinic cell differ significantly from those in the WS_2 hexagonal unit cell, requiring the nearest W−W interatomic distances along the *a* and *c* axes to change significantly, that is, from 0.38 nm in WO_3

Received: August 26, 2018
Accepted: March 26, 2019
Published: March 26, 2019

DOI: 10.1021/acsnano.8b06515
ACS Nano 2019, 13, 3896−3909

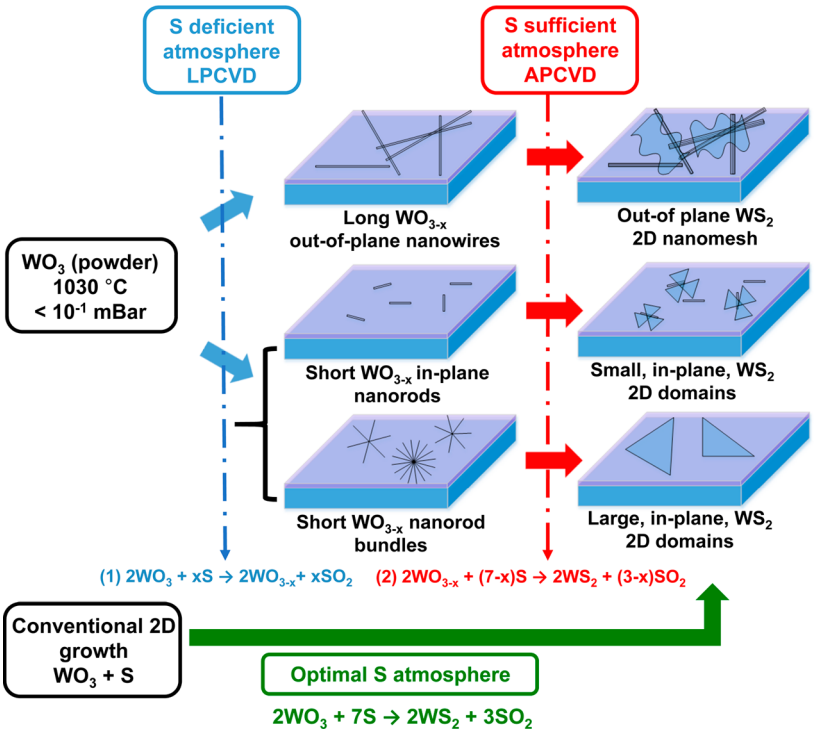

Figure 1. Flow-chart describing the decoupled, two-stage strategy for synthesis of crystalline WS_2 nanophases starting from WO_3 and sulfur powders as precursors, mapped onto a two-stage reaction. Stage 1 (blue arrows), a low-pressure CVD (LPCVD) process, where partial reduction of WO_3 takes place in an S-deficient atmosphere, leads to the formation of various WO_{3-x} morphologies, that is, long out-of-plane nanowires, short in-plane nanorods, and short nanorod bundles. From each of these morphologies, distinct, pure WS_2 nanophases result after sulfurization in stage 2 (red arrows), such as an out-of-plane 2D nanomesh, as well as 2D in-plane domains of various sizes; this is an atmospheric pressure CVD (APCVD) process. Conventional in-plane 2D domain growth, obtained by WO_3 fast reduction in an optimal S atmosphere, is indicated by the green arrow.

to 0.315 nm in WS_2 along the *a* axis and from 0.38 nm in WO_3 to 0.62 nm in WS_2 along the *c* axis.[20] An intermediate WO_{3-x} suboxide stage, which would allow for partial displacement of W atoms and facilitate the conversion, was demonstrated in the growth of WS_2 nanotubes,[21,22] but has never been exploited so far for 2D growth. In general, in conventional in-plane (parallel to substrate) 2D growth, where WO_3 is rapidly reduced and sulfurized in an optimal S atmosphere, a couple of studies have reported oxi-sulfides instead of suboxides as the reaction intermediates, though no common growth mechanism has emerged.[9,23]

In conventional 2D growth *via* CVD, the operational window for optimal, monolayer growth is very narrow. In general, it is necessary to avoid premature mixing of the WO_3 with S vapor as this interferes with WO_3 sublimation, causing a deficit of W precursor and, hence, precluding WS_2 formation on the growth substrate.[24] If S is introduced too late, however, an excess of WO_3 precursor will arrive at the substrate resulting in the growth of thick multilayer WS_2 or W nanowires.[24,25] The question is then: How early (late) is too early (late)? Hu *et al.*[25] reported that introducing S 6 min before the WO_3 precursor reaches the target temperature provides optimal conditions for maximum size growth of WS_2 (with ~150 μm lateral size of domains). However, if S was introduced only 4 min before the WO_3 precursor reaches the target temperature, the WS_2 domains became thicker and much smaller (20−30 μm in lateral size).[25] In contrast, in most of the reported works for CVD growth of WS_2, S was introduced simultaneously with WO_3,[26−34] corresponding to the case of "too late" in refs 24 and 25. It is clear that the conditions for optimal CVD growth of monolayer WS_2 are very sensitive to the specific CVD configuration. It is thus of interest to explore if other 2D growth regimes exist that rely less on the precise timing of S and WO_3 introduction into the gas phase.

Here, we intentionally created an initial S-deficient environment, in order to decouple the overall CVD reaction into a two-stage process. We thus took the decoupling idea to the extreme and created a WO_{3-x} phase with nanorod morphologies as precursors, which we then sulfurized. This approach has similarities with the concept underpinning the synthesis of WS_2 nanotubes, obtained by sulfurization of WO_{3-x} nanowires.[35,36] As a result of stage decoupling, which does not occur in conventional CVD of 2D TMDs, we were able to show that 2D growth of WS_2 can occur *via* the $WO_{2.92}$/$WO_{2.9}$ suboxides and hence demonstrate a viable suboxide path to 2D growth. This approach also allowed us to demonstrate a facile, tunable CVD route capable of flexibly producing in a single process stream a variety of WS_2 phases, spanning from one-dimensional (1D) to 2D, as well as grown in-plane or out-of-plane. Through this process, a 2D nanomesh, described as an out-of-plane network of webbed 2D sheets (of mainly one to three WS_2 layers) with large, μm-range lateral domain size was created; this is the ultimate stage in an evolutionary process started with the $WO_{2.92}$/$WO_{2.9}$ nanowires, from which WS_2 nanotubes with WO_{3-x} cores formed, which then gave rise to 2D sheets as the S-mediated reduction process progressed. The tunability and functionality of this class of WS_2 materials are demonstrated through comparative investigations of the optical properties of representative phases obtained at progressing stages: the 1D,

DOI: 10.1021/acsnano.8b06515
ACS Nano 2019, 13, 3896−3909

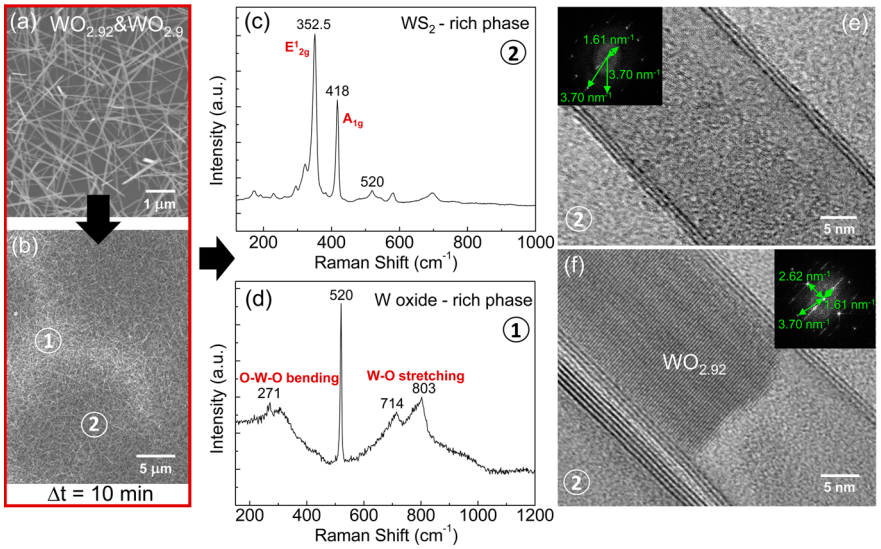

Figure 2. Long, out-of-plane nanowires of $WO_{2.92}$ and $WO_{2.9}$ suboxide, Magnéli phases leading to the formation of few-layer multiwalled nanotubes with suboxide cores. (a, b) SEM of pure WO_{3-x} nanowires before and after 10 min of sulfurization, respectively. The example in (b) shows a predominant WS_2-rich phase (labeled "2"), interspersed with a residual pure WO_{3-x} phase (labeled "1"). Their respective Raman spectra (excitation wavelength of 532 nm) are shown in (c) and (d). (e, f) TEM images of the sulfurized nanorods showing multiwalled nanotubes of large diameter and relatively few layers. In (e), the highlighted FFT inset vectors correspond to 0.27 nm, the distance between the (100) planes of 2H-WS_2 crystals, and to 0.62 nm, the van der Waals intertube distance. In (f), the $WO_{2.92}$ suboxide core nanowire is still visible. The FFT inset highlights, in addition to the distances identified in (e), 0.382 nm along the long axis of the suboxide core, which corresponds to the distance between the (010) planes of monoclinic $WO_{2.92}$.

nanotube-based phase *vs* an intermediary phase of mixed 1D/2D content and, finally, *vs* the 2D nanomesh. We thus measured (i) reflectivity and correlated it with optical excitations, as well as (ii) nonlinear optical properties, that is, second harmonic generation (SHG) and onset of saturable absorption, in the three types of materials. All the WS_2 materials in the class showed strong nonlinear optical properties, with the 2D nanomesh being most SHG active. Finally, we showed that in this decoupled, two-stage growth, in-plane 2D mono- and few-layer WS_2 can be grown in a "self-seeding and feeding" process, where the nucleation sites and the source of precursor material are provided by the same phase; unlike in heterogeneous seeding processes demonstrated so far, where organic molecular species were used as seeds.[6,8,37]

RESULTS AND DISCUSSION

Figure 1 presents the flowchart for the catalyst-free CVD processes discussed in this work, showing the inter-relation, and contrasting differences, between the conventional growth of 2D domains[38] and the processes and phases enabled by the decoupling of the overall reaction into two distinct stages.

During 2D growth the reaction ideally happens in the vapor phase: WO_3 is partially reduced by the sulfur vapor to form volatile WO_{3-x} suboxide species, which are then further sulfurized to form large crystalline domains of mono- and few-layer WS_2 on substrates. However, the reaction occurs too fast for any intermediary stages to be observed and confirmed. In contrast, here we intentionally decouple the reaction into two stages. In our decoupled reaction, we engineered a first reaction stage (WO_3 partial reduction performed below atmospheric pressure, blue arrows on Figure 1) where the vapor phase is S-deficient, leading to the initial growth of 1D WO_{3-x} morphologies, such as nanowires or short nanorods. Then, in a second stage (sulfurization at atmospheric pressure, red arrows on Figure 1), the nanowires/nanorods are reacted in an S-rich atmosphere for varying amounts of time, ultimately leading to the formation of pure WS_2 nanophases characterized by the emergence of 2D domains and crystallites. It is apparent (see Figures 2−5) that the type of 1D suboxide morphology in the first stage and the period of sulfurization in the second stage control the resulting WS_2 nanophases: (i) using long, out-of-plane WO_{3-x} nanowires as precursors yielded WS_2 nanotubes, a hybrid 1D/2D film, or an out-of-plane 2D nanomesh, while (ii) short nanorod precursors yielded in-plane 2D WS_2 growth. By performing further structural analysis, we were able to demonstrate that the two growth stages map onto the two hypothesized reaction stages:[39,40] (i) $2WO_3 + xS \rightarrow 2WO_{3-x} + xSO_2$ and (ii) $2WO_{3-x} + (7-x)S \rightarrow 2WS_2 + (3-x)SO_2$. We thus confirm this two-stage reaction mechanism and the involvement of suboxides as intermediary subspecies.

WO_{3-x} nanowire/nanorod morphologies were obtained in the first reaction stage (Figure 1), using a home-built low-pressure CVD (LPCVD) reactor involving a horizontal furnace with a temperature gradient (Methods and Supporting Information, Figure S1). The boat containing the WO_3 precursor was placed in the center of the furnace, within its constant temperature zone; temperature was ramped to 1030 °C, at a pressure below 10^{-1} mbar, and then held constant for 20 min, to ensure sufficient sublimation. Subsequently, the sulfur powder, placed in a boat 40 cm upstream of the WO_3 boat, was heated to 200 °C over 10 min and then co-evaporated together with the WO_3 over 15 min. Another boat with four pockets, each 2 cm long, and containing SiO_2/Si substrates, was placed 6 cm downstream of the WO_3 boat, in a zone with a temperature gradient. Only argon was used for transporting the WO_3 and sulfur vapor to the SiO_2/Si substrates. According to the temperature profile of the furnace, there is a temperature drop of about 60 °C between each substrate-containing pocket. This enabled a W precursor

DOI: 10.1021/acsnano.8b06515
ACS Nano 2019, 13, 3896−3909

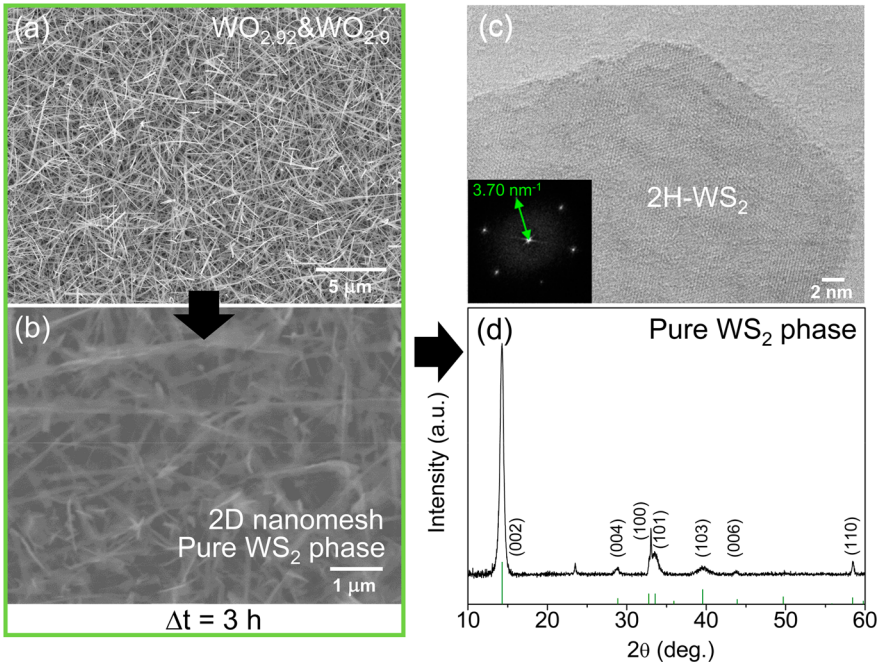

Figure 3. Full sulfurization of long, out-of-plane $WO_{2.92}$ and $WO_{2.9}$ suboxide nanowires, shown in (a), leads to a pure WS_2 2D nanomesh, shown in (b). The sulfurization was typically performed over a period Δt of 3 h. The emergence and purity of the 2H-WS_2 phase were verified by a combination of (c) HRTEM (and associated FFT, example shown in inset) and (d) XRD, where the identified crystallographic planes are also shown. In (c), a typical WS_2 crystallite with two layers is shown.

concentration gradient across the various substrate locations,[41,42] leading to a continuous variation in the growth conditions. In contrast, the long separation distance between the S and substrate boats ensured that the S vapor concentration gradient across the Si/SiO_2 substrates can be ignored, unlike that of WO_3.

Depending on the position and temperature of the substrate relative to the W precursor, different WO_{3-x} morphologies were obtained (Figures 2 and 5, see also Supporting Information, Figure S1). (i) In the pocket furthest from the W precursor, the relatively low temperature of around 780 °C induces a low diffusion rate of the precursor, leading to the precursor being trapped at many random sites on the substrate. After the nucleation sites become saturated with precursor, further trapping of precursor results in crystallization and growth. A high carrier gas flow rate (~150 sccm) promotes mass transfer, which contributes to a fast crystal growth rate[41] leading to the formation of long, out-of-plane nanowires (Figures 2 and 3), and Supporting Information, Figure S2). (ii) The pocket closer to the WO_3 boat was reached by a higher concentration of W precursor, while also being held at the highest temperature, 1000 °C, of all the substrates. In general, a high temperature induces a high diffusion rate of the precursor, favoring film growth. On the other hand, too high a temperature causes large thermal turbulence, resulting in an instability of as-grown nucleation sites[43] and hindering growth. Hence, under these conditions of temperature and W precursor concentration short nanorod bundles were formed (Figure 5d, and Supporting Information, Figure S2). (iii) In between these high and low temperature regimes, in a pocket located in an intermediate position at about 960 °C, the decrease in precursor concentration results in a crystal growth rate slow-down: The positive influence of a high flow rate balanced by a moderate diffusion rate of precursor at a moderate temperature leads to stable, while slow, crystal growth under thermodynamic control. Hence, short, in-plane nanorods could be grown (Figure 5b).

We now analyze the outcome of stage 2—sulfurization—of the decoupled reaction diagrammatically shown in Figure 1, where each of the three nanowire/nanorod morphologies described above are reacted with sulfur.

WO_{3-x} Long Nanowires as Precursors. Figure 2a shows the WO_{3-x} nanowires grown on the SiO_2/Si substrate (Methods): Their diameters fall in a narrow range, 10−30 nm, and they can reach several microns in length. A combination of X-ray diffraction (XRD) (Supporting Information, Figure S2) and high-resolution transmission electron microscopy (HRTEM) showed that $WO_{2.92}$ ($W_{25}O_{73}$) and $WO_{2.9}$ ($W_{20}O_{58}$) are the phases encountered in the nanowires (Supporting Information, Figure S2a−d). Indeed, fast Fourier transform (FFT) analysis of the examples given in Supporting Information, Figure S2c,d show periodicities along the long axis of the nanorods that correspond to 3.82 and 3.78 Å, respectively, which are in good agreement with the b lattice parameters of monoclinic $WO_{2.92}$[44] and $WO_{2.9}$.[45] Both of these suboxides belong to the substoichiometric Magnéli phases, which have the series formula of W_nO_{3n-2}.[46] Most importantly, both suboxides are nonvolatile (see Methods) but can be reduced further into volatile suboxides (see discussion below) at the temperatures used in the subsequent sulfurization stage from Figure 1; this is consequential, as it strongly influences the type of WS_2 nanostructures that can be obtained by sulfurization, as demonstrated in the following.

The as-grown $WO_{2.92}/WO_{2.9}$ nanowires on SiO_2/Si were sulfurized as described in Methods, at atmospheric pressure (an APCVD process), in the first instance over ~10 min. Figure 2b shows a scanning electron microscopy (SEM) image of the resulting post-sulfurized nanowires: Two types of material, with different electronic contrast, can be observed.

DOI: 10.1021/acsnano.8b06515
ACS Nano 2019, 13, 3896−3909

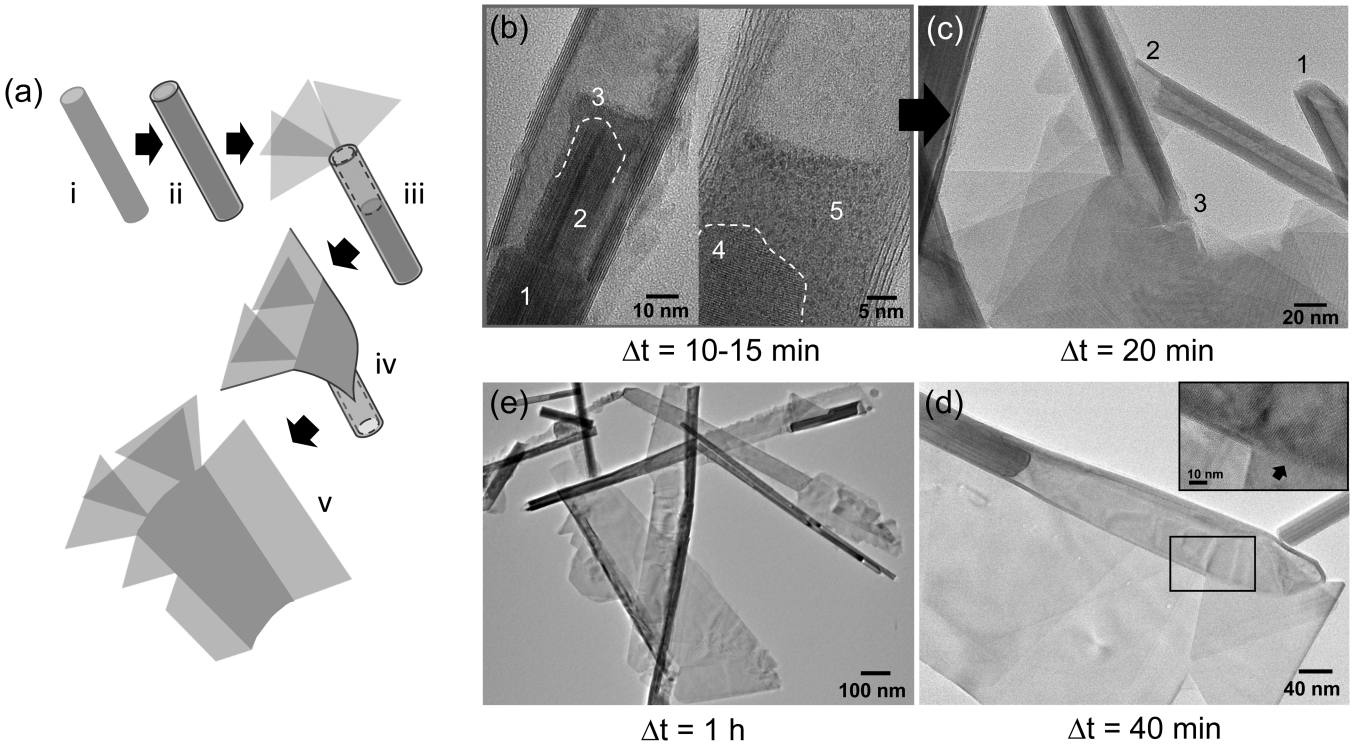

Figure 4. Evolution with sulfurization time, Δ*t*, of the suboxide cores into WS_2 nanophases. (a) Several stages (i–v) were identified, mapping onto representative TEM images (c–e): $WO_{2.92}/WO_{2.9}$ nanowires (i) become covered with few-layer nanotube sheaths (ii) in a layer-by-layer conversion of suboxide into 2H-WS_2; (iii) $WO_{2.92}/WO_{2.9}$ core suboxide reduces to a lower stoichiometry, volatile suboxide which leaves the tubes and nucleates into 2H-WS_2 sheets at the tube apex; (iv) WS_2 2D domains grow by epitaxy on the body of the nanotubes, which are then subjected to gradual opening; (v) finally, nanotubes fully open and merge with extended 2D 2H-WS_2 sheets. (b) The emergence of the volatile suboxide phase, with 1, 2, and 4 showing crystalline suboxide, while 3 and 5 show regions of reduced crystallinity (boundary between the two regions shown with dashed line). (c) WS_2 nanotubes (2 and 3) have no suboxide filling and nucleated 2H-WS_2 sheets at the apex of the tube, while (1) shows the breached end of a nanotube through which filling material can escape. (d) Large 2D WS_2 sheets nucleated all along the body of the nanotube, which is still partially filled. The unfilled region shows gradual nanotube opening, while the zoomed area highlighted in the inset figure shows the nanotube layers fusing with the grown 2D sheets. (e) Extended, micron-wide 2D sheets grown all along the nanotubes' bodies.

The brighter areas have very broad Raman peaks at 271, 326, 714, and 803 cm^{-1} (Figure 2d). Peaks centered at 714 and 803 cm^{-1} are attributed to W–O stretching vibration modes, while the two lower peaks at 272 and 326 cm^{-1} are induced by O–W–O bending vibration modes,[47] identifying these regions as nonconverted, pure suboxide phases. Raman spectroscopy confirms that the regions that appear dark in both optical and SEM images are 2H-WS_2 (Figure 2c, and Supporting Information, Figure S3): The 352.5 and 418 cm^{-1} peaks correspond to the E^1_{2g} and A_{1g} vibrational modes, respectively, of this phase, while their spectral distance of ~65.5 cm^{-1} shows that the phase is made up of few-layer WS_2 nanotubes.[48] HRTEM (Figure 2e,f) confirms that the sulfurized nanowire-shaped morphologies are actually the suboxide nanowires transforming into multilayered WS_2 nanotubes. The HRTEM images and their associated FFTs (inset panels) give a spacing between the layers of the nanotubes of about 0.62 nm, consistent with the (002) *d*-spacing within a multilayer 2H-WS_2 crystal. The nanotubes are partially filled with $WO_{2.92}$ or $WO_{2.9}$ suboxides cores, as demonstrated by Figure 2f; the associated FFT identifies the core inside the nanotube as $WO_{2.92}$ based on its *b* lattice parameter. However, despite the presence of W suboxide cores inside some of the nanotubes, Raman spectroscopy does not detect any of their W–O vibration modes; a similar behavior was previously reported for other core–shell systems.[48,49] The coexistence of WS_2 nanotubes and W suboxides is reminiscent, in this respect, of the work from Tenne's group on the synthesis of MoS_2 and WS_2 nanotubes.[36,50] Therefore, it is reasonable to assume that the WS_2-rich areas from Figure 2b are actually a proto-stage of the growth of WS_2 nanotubes around the suboxide nanowire cores.

In contrast to here, previous works on the synthesis of WS_2 nanotubes mainly used W oxide nanowires formed by the hydrothermal method, which primarily consisted of the nonvolatile, low-stoichiometry $WO_{2.72}$ ($W_{18}O_{49}$) phase; this is the so-called reduction-resistance phase and will not undergo further reduction.[36,51] In their work based on vapor phase reaction in a fluidized bed reactor, Tenne *et al.*[35] have found that several intermediate, higher stoichiometry suboxides could also be present during the formation of their WO_{3-x} nanowires; however, the nonvolatile $WO_{2.72}$ was identified as the resulting stable phase in the nanowires, which then served as a template for the subsequent sulfurization reaction yielding WS_2 nanotubes. The transformation of the suboxide nanowires into WS_2 nanotubes is then diffusion-controlled, and such conversion takes place slowly and layer-by-layer relying on the sulfur diffusing to the core. In our case, however, with further annealing in a S-rich environment, the high stoichiometry $WO_{2.92}$ or $WO_{2.9}$ nanowire cores, rather than being sulfurized layer-by-layer, are able to transform to lower stoichiometry, volatile WO_{3-x} phases; $3 - x$ could be 2.89 (*i.e.*, $WO_{2.89}$

DOI: 10.1021/acsnano.8b06515
ACS Nano 2019, 13, 3896–3909

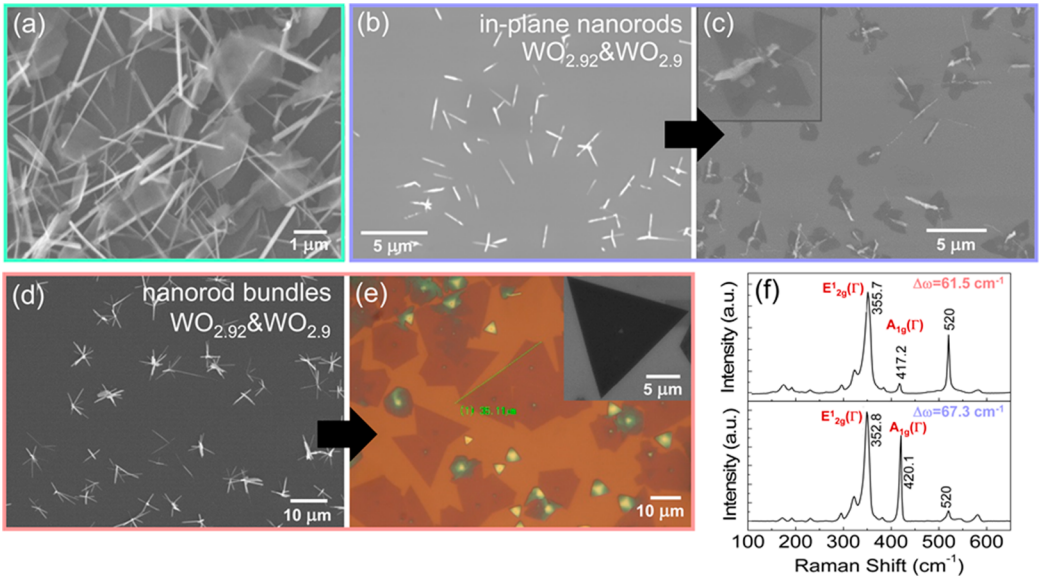

Figure 5. Effect of sulfurization of sparse $WO_{2.92}/WO_{2.9}$ nanorods revealing seeded growth of in-plane 2D 2H-WS_2 domains. (a) Sulfurization of low-density, out-of-plane nanowires leads to extended and more separated WS_2 2D crystallites; shown by SEM. (b, c) In-plane, individual, short nanorods lead to seeded, root growth of polygonal domains of multilayered WS_2; shown by SEM. (d, e) Bundles of short nanorods lead to seeded, in-plane growth of larger single-layered 2D WS_2 domains: (e) is a bright field, optical image, while (d) and inset of (e) are SEM images. (f) Raman spectroscopy (at 532 nm excitation) of single-layered WS_2 from (e), in top panel, and of multilayered WS_2 from (c), in bottom panel. The spectral distance $\Delta\omega$ between the E^1_{2g} (Γ) and A_{1g} (Γ) vibrational modes of WS_2 is used to identify the number of layers within the 2D domains.

$(W_{19}O_{55})$)[52] or in the range 2.72−2.83 that contains volatile phases.[36,51,52] Such phases can then escape through the open/defective ends of the nanotubes. This results in a higher conversion rate to WS_2, which can then nucleate and grow as 2D sheets outside the nanotubes (see Figure 4 and related discussion).

Hence, sulfurization, in the first stage, produces single- or few-wall WS_2 nanotubes, with partial cores of suboxide still present; the layer-by-layer conversion does not continue long enough to involve full transformation of the $WO_{2.92}/WO_{2.9}$ cores into the nanotube phase as suboxide material leaves the nanotubes. In contrast, from the nonvolatile $WO_{2.72}$ phase, thick multilayered nanotubes with empty cores are generated. For instance, as shown by HRTEM in Figure 2e,f, we could obtain trilayer WS_2 nanotubes of diameter more than 25 nm using the $WO_{2.92}/WO_{2.9}$ precursors, while from the lower stoichiometry, reduction-resistant, $WO_{2.72}$ precursor, nanotubes of around 20 nm in diameter have more than 10 layers.[53]

In order to determine the ultimate effect of the sulfurization, the long, out-of-plane nanowires were continuously sulfurized under the same conditions for a large period, typically <3 h. A final morphology was then achieved: Figure 3b shows a 2D nanomesh structure of webbed 2D crystallites, extending out-of-plane for microns (up to ∼10 μm), and with a very large specific surface area. Figure 3c presents the TEM image, and associated FFT, of a typical crystallite, which has a hexagonal lattice structure with 0.27 nm periodicity resulting from the (100) planes of 2H-WS_2,[54] and two layers are visible. A representative nanomesh XRD spectrum is shown in Figure 3d. All the diffraction peaks are indexed relative to the hexagonal *P*63/*mmc* space group, indicating that the structure of the WS_2 phase is 2H-WS_2, while there is almost no trace of W suboxide peaks. The sharpness of the peaks demonstrates the good crystallinity of the sample overall.

Between these two extremes, the WS_2 material can be evolved in a continuous manner, with a variable proportion of nanotube (1D) and 2D phases, as depicted by stages (i−v) in Figure 4a. Figure 4b−e shows TEM images of the material at different stages of sulfurization. After the formation of an initial nanotube sheath around the $WO_{2.92}/WO_{2.9}$ cores, volatile WO_{3-x} suboxide (obtained by subsequent reduction of the nonvolatile $WO_{2.92}/WO_{2.9}$) forms and then leaves the nanotubes through their open ends (or, alternatively, through wall defects that sometimes develop) (Figure 4b) and nucleates 2D crystallites at the nanotubes' ends (Figure 4c). The nanotube exterior provides an ideal surface for subsequent epitaxial growth of 2D domains, the evolution of which is often accompanied by a gradual opening of the nanotubes, presumably catalyzed by stresses on the nanotube bonds induced by the 2D growth (Figures 4d,e). "Un-zipping" of WS_2 nanotubes was previously reported, though based on Li intercalation.[55] Once opened, the 2D sheets and the nanotube edge can also fuse, as shown in the inset of Figure 4d. Figure 4a shows diagrammatically the various stages of this evolution, from $WO_{2.92}/WO_{2.9}$ nanowires, through WS_2 nanotubes (with partial suboxide cores), then hybrid 1D/2D materials, and finally into a pure WS_2 2D nanomesh.

The formation of the pure WS_2 2D nanomesh, with extensive 2D content (Figure 3b) is in contrast to other recently reported hybrid phases which were a mixture of 2D WS_2 crystallites and WO_3[56] or had a mixed 1D-2D character, with a main nanowire phase and a small 2D phase content.[57] Temperature-dependent conductivity measurements on our pure WS_2 2D nanomesh (Supporting Information, Figure S5) demonstrate the semiconducting nature of this phase, while an activation energy $E_a \approx 0.33$ eV indicates thermally activated transport, *via* a defect band, around (and just below) room temperature. Further optical properties of this nanomesh are presented in the last section.

DOI: 10.1021/acsnano.8b06515
ACS Nano 2019, 13, 3896−3909

WO_{3-x} Short Nanorods as Precursors. Figure 5a shows the results of atmospheric pressure sulfurization in a region of lower density of suboxide nanowires. It is clear that less dense nanowires yield relatively larger and more separated, out-of-plane 2D WS_2 crystallites. This suggests that if the W suboxide nanowires are well-separated and oriented in plane, they may be used as seeds for the growth of in-plane 2D WS_2 films.

Hence, as-grown in-plane, single, short $WO_{2.92}/WO_{2.9}$ nanorods on SiO_2/Si were similarly sulfurized (Methods), and Figure 5b,c shows the result of such a scenario: In-plane, triangular, few-layer 2D domains grow from the nanorods at their basis. This root growth is enabled by the same transformation stage sequence shown in Figure 4a, with the volatile suboxide emerging from the WS_2 nanotubes and converting to WS_2 domains that nucleate directly onto the SiO_2/Si substrate, thus keeping the material localized around the original nanorod. Raman spectroscopy confirms that the domains grown are WS_2, albeit thicker than monolayers (Figure 5f and Supporting Information, Figure S5b). This result demonstrates the feasibility of using W suboxide nanorods as seeds for the 2D in-plane growth of WS_2. Seeded growth of 2D WS_2 domains has been studied by using either large aromatic molecules (*e.g.*, perylene-3,4,9,10-tetracarboxylic acid tetra-potassium salt (PTAS))[6,8,37] or patterned oxide precursor particles[58] as externally introduced nucleation sites, over which W- and S-carrying species were subsequently introduced. However, in our case, the seed is provided by the suboxide nanorods without introducing other external contamination. Moreover, the 2D domain growth can be treated as a "self-seeding and feeding" one, in which the suboxide nanorods provide both the nucleation sites and the W precursor feedstock for the growth of layers.

In "self-seeding and feeding", the size of the in-plane 2D domains that can be grown is constrained by the amount of W precursor available in the seeds. Hence, larger 2D domains could be grown by increasing the amount of precursor delivered by the nanorod seeds. Therefore, as shown in Figure 5d, we used clusters of short W suboxide nanorods as the precursors in the sulfurization stage; these clusters have also been confirmed by XRD to be a mixture of $WO_{2.92}$ and $WO_{2.9}$ phases (Supporting Information, Figure S2). Optical/SEM images (Figure 5e) and Raman characterization (Figure 5f and Supporting Information, Figure S5a) show that their sulfurization resulted in the growth of in-plane triangular domains of predominantly monolayer 2D WS_2 domains. These domains are also substantially larger than the multilayer domains shown in Figure 5c obtained from single nanorods as seeds. As the amount of precursor and distance to the substrate increased compared to the case of single, in-plane nanorods, the WS_2 domains now grow *via* a mixture of reaction mechanisms: Root growth (as observed in Figure 5c) competes with gas-phase transport and reaction. Indeed, by the reduction of $WO_{2.92}/WO_{2.9}$ to lower-stoichiometry, volatile WO_{3-x} phases (as *per* the mechanism depicted in Figure 4a), the latter can readily transfer to vapor phase as *in situ* precursor to supply the conversion reaction. The W suboxide seed growth demonstrated above is distinct from a recently shown process where WS_2 nanotubes were sublimated in order to induce WS_2 monolayer growth by vapor phase transport and surface diffusion.[59,60]

"Self-seeding and feeding" from precursor nanowires could potentially be harnessed by controlling nanowire growth *via* substrate engineering, thereby allowing for the positional control of WS_2 domain growth, while the limited feedstock of material would limit the resulting domain size and facilitate patterning. For example, when sapphire, a substrate frequently used in TMD growth,[19,61−63] with unstable orientations is annealed at high temperature, it spontaneously becomes periodically faceted.[64] Specifically, the mis-cut C plane (0001) (2° toward $[1\bar{1}00]$) facets into L-shaped nanosteps, while the M plane $(10\bar{1}0)$ facets into V-shaped nanogrooves. It has been demonstrated that various types of nanowires (*e.g.*, of ZnO,[65] GaAs,[66] or GaN,[67] *etc.*) could be grown with a good degree of alignment on both these facets. Furthermore, tungsten oxide nanorods have been reported to epitaxially grow on mica using a simple vapor−solid growth process.[68]

Figure 6 shows, as a corollary, the various pathways uncovered so far in previous works for the 2D growth of

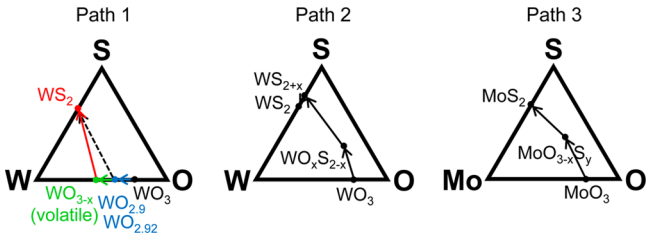

Figure 6. W−O−S ternary phase diagrams showing reaction pathways to 2D 2H-WS_2 during CVD growth from WO_3 and sulfur precursors. Path 1 (left diagram) describes a reaction mechanism *via* the nonvolatile $WO_{2.92}/WO_{2.9}$ phases and their subsequent reduction to lower stoichiometry, volatile WO_{3-x} phases, as shown in this work. 2D growth corresponds to the blue-green-red path, while the black, dotted path corresponds to 1D (nanotube) phase synthesis. Paths 2 (middle) and 3 (right), identified in conventional 2D growth of WS_2, highlight reaction mechanisms where oxi-sulfides are the intermediary compounds.

TMDs from transition-metal trioxides.[9,23,69,70] On paths 2 and 3, corresponding to conventional 2D growth, W or Mo oxi-sulfide nanoparticles first formed and were adsorbed on substrates as nucleation cores for further reduction. No common growth mechanism has emerged from these studies, the various proposed scenarios being inconsistent with each other and resulting in different and complex reactions paths. In contrast, path 1 highlights the suboxide route to 2D growth demonstrated in this work. A common mechanism can explain both in-plane and out-of-plane 2D growth processes which rely on the initial formation of $WO_{2.92}$ and $WO_{2.9}$ (blue arrow on the W−O−S phase diagram). Our process of 2D WS_2 synthesis always starts with the formation of few-layer WS_2 nanotubes around the $WO_{2.92}/WO_{2.92}$ cores. Nanotube formation is controlled by the specific crystallographic structure of the Magnéli suboxide phases which contain crystallographic shear (CS) planes (Supporting Information, Figure S6) created as result of oxygen vacancies introduced by reduction. At the atomic level, the shear process is equivalent to the diffusion of an atom to a neighboring lattice vacancy; however, it was previously proposed that the octahedra hop as a whole during the process leads to the formation of edge sharing octahedral units, that is, the CS planes (Supporting Information, Figure S6), as opposed to corner sharing ones.[20,71] While the reaction progresses, regions of such edge-sharing octahedral units develop across the crystal. The edge-sharing octahedral units in $WO_{2.92}$ and $WO_{2.9}$ are now similar to the 1T-WS_2 octahedral structure (Supporting

DOI: 10.1021/acsnano.8b06515
ACS Nano 2019, 13, 3896−3909

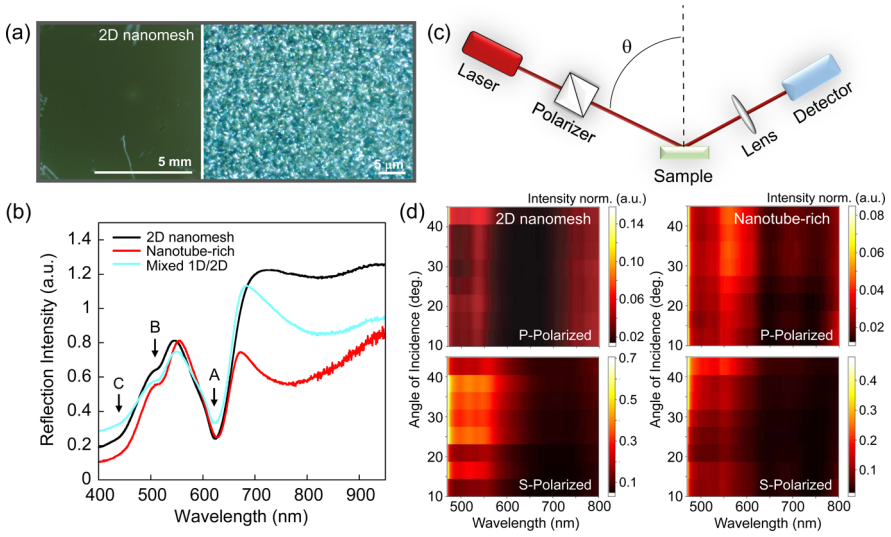

Figure 7. Linear optical properties of the class of out-of-plane WS_2 phases, showing representative phases: nanotube-rich (1D); intermediary, with mixed 1D/2D content; and 2D nanomesh. (a) Left, a photograph of the 2D nanomesh; right, a dark-field microscopy image from the 2D nanomesh, *via* a ×100 objective. (b) Reflectivity spectra obtained in bright-field microscopy at normal incidence with unpolarized light, from the three types of phases. (c) Experimental setup for the angular-dependent reflectivity measurements shown in (d). (d) Reflectivity spectral maps, as a function of angle of incidence, from the nanotube-rich (1D) and 2D nanomesh samples, and for P- and S-polarized light.

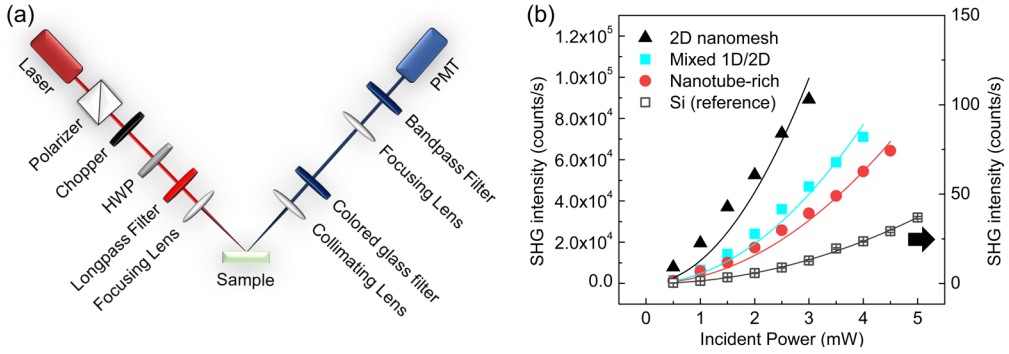

Figure 8. Nonlinear optical properties of the class of out-of-plane WS_2 phases, showing representative phases: nanotube-rich (1D); intermediary, with mixed 1D/2D content; and 2D nanomesh. (a) Experimental setup. HWP designates a half wave-plate and PMT stands for photomultiplier tube. (b) SHG intensity as a function of the incident power, for the three types of WS_2 samples (left *Y* axis) and for the Si substrate used as a reference (right *Y* axis, indicated by black arrow). Error bars representative for the experiment can be seen in the low signal data from Si; these are too small to be visible on the WS_2 data. The continuous lines are fits to quadratic functions characteristic of SHG behavior (R^2 = 0.91; 0.97; 0.98; and 0.998 for the 2D nanomesh, mixed 1D/2D content, nanotube-rich (1D) samples, and Si substrate, respectively); deviations of data from these lines demonstrate onset of saturable absorption.

Information, Figure S6). As the sulfurization proceeds, O atoms are released from the lattices of the Magnéli phases and replaced by S atoms, leading to the expansion of the unit cell along the *c* axis, while the W−W bond length in the edge-sharing octahedral units of $WO_{2.92}/WO_{2.9}$ is already very similar to that of 2H-WS_2 (Supporting Information, Figure S6). This process is depicted by the dotted arrow on the W−O−S phase diagram of path 1 on Figure 6. This $WO_{2.92}/WO_{2.9}$ route is supported by recent findings that starting directly from $WO_{2.9}$ as a precursor (as opposed to WO_3 and without controlling the intermediary reaction) promotes 2D growth of larger and more uniform domains of WSe_2/WS_2.[27,72] Finally, in our scenario, the 2D WS_2 sheets always form after the formation of the nanotubes, and the reaction path is depicted by the green-red path on the W−O−S phase diagram; thus, the residual $WO_{2.92}/WO_{2.9}$ from inside the nanotubes converts into lower stoichiometry, volatile Magnéli WO_{3-x} phases, which can escape the nanotubes and nucleate as WS_2 outside them, and then evolve into extended 2D sheets as described in Figure 4a.

Finally, we investigated some of the opportunities afforded by the tunability of the relative 1D to 2D content of the material. Hence, we measured and contrasted the linear optical properties (Methods) of out-of-plane, nanotube-rich and 2D nanomesh samples, as well as an intermediary sample with mixed 1D/2D content, and related them to the relevant optical excitations that can occur in them. The nonlinear optical behavior of these three samples was subsequently tested (Methods). Figure 7a, left, shows a photograph of the 2D nanomesh sample, demonstrating its homogeneity over a large area (>8 × 8 mm^2), while at a magnification ×100, randomly distributed structures appear well resolved in dark-field illumination (Figure 7a, right). In order to obtain reflectance spectra, illumination was switched to bright-field, and measurements were taken at normal incidence with unpolarized light. Figure 7b shows characteristic optical reflection

DOI: 10.1021/acsnano.8b06515
ACS Nano 2019, 13, 3896−3909

spectra from all three samples: (i) nanotube-rich, (ii) with intermediary 1D/2D content, and (iii) the 2D nanomesh, normalized to the reflectivity of the SiO_2/Si substrate. Over the 400−650 nm range, all three samples exhibit dips in reflectivity, marked with A, B, and C, corresponding to increased extinction. These can be attributed to excitonic resonances for A and B and optical absorption between density of states peaks in the valence and conductions bands for C, in agreement with previous reports.[73,74] For the nanotube-rich sample, these spectral features are located at 628, 521.7, and around 450 nm, respectively, and red-shifted relative to the intermediary 1D/2D content sample and the 2D nanomesh. The intermediary, mixed 1D/2D content sample has spectral features close to the 2D nanomesh, owing to its large 2D content, though its nonlinear optical properties are distinctive compared to the other two samples in the series (see Figure 8b). For the 2D nanomesh, A, B, and C are located at 622.5, 515.8, and ∼443 nm, respectively, in good agreement with spectra of mechanically exfoliated mono- and bilayer WS_2 sheets,[73] indicating the prevalence of mono- and bilayer WS_2 sheets in our material; in comparison, thicker 2D sheets have their spectral features red-shifted.[73] The broadening of the A, B, and C features relative to those measured on mechanically exfoliated WS_2 2D layers of well-defined thickness[73] likely reflects the (thickness) polydisperse nature of all three samples as well as the presence of defects in these materials. Above 700 nm, in the nanotube-rich sample, there is a very broad spectral feature centered around 760 nm, and a counterpart can be seen around 840 nm in both the 2D nanomesh sample and the one with mixed 1D/2D content. Due to their broadness and the large spectral difference (∼80 nm) between their location for the three samples, as well as the lack of known possible excitations in this spectral region in (perfect) laterally extended WS_2 sheets (mono- or few-layer) or bulk crystals, it is more likely that these spectral features are caused by geometrical/morphological characteristics of the two samples. For nanotubes of diameters comparable with the excitation light wavelength and with many layers (*i.e.*, creating a material with high refractive index), cavity mode resonances can be excited, for example, 760 nm excitation can excite cavity modes in a 70 nm radius WS_2 multilayer nanotube, while by decreasing the nanotube radius, the wavelength of the light that can excite cavity modes decreases.[74] Consequently, as the nanotube diameters in our nanotube-rich sample are in the 10−30 nm range, no cavity resonances can be excited in the spectral range investigated here, and such excitations can thereby be ruled out. Most likely, the broad spectral features are sample geometry or morphology related, for example, the result of a collective behavior of the material. Tentatively, we propose an explanation based on the nanotube-rich material and the 2D nanomesh being approximated as homogeneous films with distinctive effective refractive indices, n_{eff}, of about 4 for the pure WS_2 2D nanomesh,[74] and moving closer to 2 for the nanotube-rich sample where the cores of the nanotubes are air or WO_{3-x}.[75] In this approximation, the broad spectral features in the near-infrared region can be interpreted as antiresonances (manifested as dips in reflectivity) resulting from interference of light reflected from the top and bottom interfaces of the effective WS_2 film, and the wavelength at which an antiresonance occurs increases with n_{eff}. In addition, the morphology of the film can affect how pronounced an antiresonance is, and it is expected that the homogeneous film approximation works better for the nanotube-rich sample than for the 2D nanomesh where the multiple 2D planes produce more scattering and higher overall reflectivity. Hence the antiresonance effect would manifest at larger wavelength and be weaker in the 2D nanomesh, which appears to agree with the experimental findings. More investigations are needed to clarify the origin of these broad spectral features.

Figure 7d presents spectral maps of the reflection intensity of each of the nanotube-rich and 2D nanomesh samples, as a function of the angle of incidence, where the measurements were taken with polarized light using the setup from Figure 7c (Methods). For both P-polarized lights (upper panels), the spectral signatures appear to correlate well with those in Figure 7b, including the A, B, and C features, and do not change significantly upon varying the angle of incidence. Consequently, these spectral signatures are specific to WS_2 as a material. For S-polarized light, the spectral maps are also modulated by the features shown in Figure 7b; however, there is a stronger contribution from the broad spectral features located above 700 nm. This suggests that the S-polarized light couples more effectively with the sample as a whole, hence these maps reflect more the geometric/morphologic characteristics of the two types of samples rather than being specific to their common WS_2 constituent material.

Because of their large second-order nonlinear susceptibility, 2D materials such as WS_2 are of significant interest for nonlinear optical devices.[17,76−79] We measured the SHG for the same three types of samples investigated in Figure 7b, in the reflection geometry, using the setup from Figure 8a. SHG is a nonlinear optical technique whereby two photons at the fundamental frequency are annihilated to create a third photon, at double the frequency. Because this frequency-doubling process is exquisitely symmetry sensitive, it is used to characterize symmetry-breaking effects, such as externally applied electric[80] and magnetic[81] fields, strain,[82] chirality,[83] localized surface electric fields,[84] and surface roughness, down to the atomic monolayer.[85]

The experiments were conducted using a fundamental (incident) light of 800 nm wavelength and 100 fs laser pulses. Figure 8b shows the SHG intensity (at 400 nm) as a function of incident power of the fundamental light (at 800 nm), for the nanotube-based (1D-rich), intermediary with mixed 1D/2D content, and the 2D nanomesh samples, respectively. As a reference, the SHG signal generated by the Si substrate, which is a centrosymmetric material with low SHG response,[86,87] is also shown. All three types of WS_2 samples are extremely nonlinear, showing between 10^4 and 10^5 larger SHG intensity than Si at a given power. It should be noted that our SHG setup is built for sensitivity, with a detector upper limit set to about 10^5 counts/s, which imposes an experimental limit on the power incident on the sample. Figure 8b also unambiguously shows the SHG response is influenced by the type of WS_2 phase making up the sample: It is lowest, though still sizable, in the nanotube sample, increases for the sample with intermediary 1D/2D mixed content, and is largest in the 2D nanomesh. Indeed, the WS_2 2D nanomesh has several symmetry-breaking attributes that favor SHG: (i) It is made of mono- to three-layer sheets, as confirmed by TEM images and location of excitonic features in the reflectivity spectra, (ii) has considerable roughness arising from the formation of 2D platelets spreading around the initial 1D skeleton (as depicted in Figure 4a), and finally (iii) WS_2, in particular, benefits from the strong electric dipole established in the unit cell and linked to strong spin−orbit interaction. It is known that SHG is

DOI: 10.1021/acsnano.8b06515
ACS Nano 2019, 13, 3896−3909

strongly enhanced in TMDs with an odd number of layers, where the unit cell lacks inversion symmetry, and is strongest in the monolayer limit,[88] and for this reason, for nonlinear optics applications, such materials are exfoliated by various methods in order to then create stacks of isolated sheets.[16,76] In the case of our WS_2 2D nanomesh, the material grows directly on the substrate as "exfoliated" sheets of mono- or low number of layers, and large quantities within a high-density film of several microns in thickness, hence favoring nonlinear optical response.

Figure 8b also shows that, while the Si reference response follows the expected quadratic curve for the SHG power as a function of the fundamental excitation power,[89] this is not the case for the WS_2 samples. All three WS_2 samples (nanotubes, with mixed 1D/2D content, and 2D nanomesh) deviate from the quadratic dependence, and the deviation is strongest for the 2D nanomesh. This can be observed visually, but is clearly reflected by the differing R^2 values of the fit curves (see caption of Figure 8b). This power-dependent divergence can be attributed to the onset of saturable absorption, which correlates with an increasing presence of edge states[90] induced by the finite lateral sizes/domains of 2D nanosheets that form when the material progresses from a 1D form to full 2D content.

The very large values of SHG and promising saturable absorption properties in these materials, in particular in the 2D nanomesh, together with the ability to be grown on insulating, transparent substrates (demonstrated here on SiO_2) point toward promising nonlinear optical applications, which will be the subject of future work.

CONCLUSIONS

In conclusion, we demonstrated the sequential growth by CVD of a wide range of nanostructured materials, ranging from 1D WO_{3-x} suboxides to WS_2 nanophases with tunable 1D to 2D content, by intentionally decoupling into two stages (first stage, partial reduction; second stage, sulfurization) a reaction from WO_3 to WS_2 in order to enhance and reveal the role played by W suboxides in CVD growth of WS_2. In this process, we created $WO_{2.92}/WO_{2.92}$ morphologies, such as nanowires and nanorods, grown in-plane (*i.e.*, parallel to the substrate) or out-of-plane of the substrate; the stoichiometry of these suboxides was found instrumental in the subsequent creation of many WS_2 polymorphs. We were, thus, able to exploit a WO_{3-x}–intermediate route that is very versatile, in that it is able to create by relatively simple tuning of the CVD growth process, and in a single process stream, a rich variety of 2H-WS_2 phases: a tunable class of materials, ranging from nanotubes, to mixed 1D and 2D WS_2 phases, to an out-of-plane (of the substrate), pure WS_2 2D nanomesh with extended 2D few-layer crystallites; as well as in-plane (parallel to the substrate), self-seeded 2D domains. Regarding the in-plane 2D WS_2 films, our study showed that their growth can be routed *via* WO_{3-x} suboxides, a different route than *via* W oxi-sulfides as previously demonstrated in conventional 2D growth. Moreover, their growth proceeds *via* a "self-seeding and feeding" mechanism from 1D $WO_{2.92}/WO_{2.92}$ nanorod precursors, which may be able to take advantage of the positional and orientational growth within the substrate that can be achieved in growth of such 1D precursors.

The CVD route enables the growth of microns-thick WO_{3-x} suboxide nanowire films and WS_2 phases with tunable 1D/2D content directly on substrates, in an evolutionary manner, and on areas of at least several cm^2 (limited here by the dimensions of our furnace). WO_{3-x} suboxide nanowire films can find their own applications as sensing materials. The morphological tunability of the WS_2 phases can be exploited to tune their optoelectronic properties. In the examples given here, the evolution from WS_2 nanotubes with WO_{3-x} cores into a pure WS_2 2D nanomesh phase results in changes in the optical absorption/reflection spectra and can provide media with tunable effective refractive index. All WS_2 nanophases in the class have very strong nonlinear optical properties, with the 2D nanomesh being extremely SHG active. Films obtained by condensation of TMD suspensions or composites of nanoscale TMD flakes with polymers have been suggested in other works for nonlinear optical applications. The 2D nanomesh demonstrated here, however, has a "ready-made" sheet-exfoliated morphology, large overall effective thickness of the film, and ability to be grown directly on optically compatible substrates (*i.e.*, insulators and transparent, as opposed to metallic), which are all important advantages in terms of ease of coupling with optical systems and devices as well as improved material stability.

METHODS

Synthesis of Nanophases and Nanostructures. A home-built setup involving a horizontal furnace with a temperature gradient (Supporting Information, Figure S1) was used to first produce a variety of W suboxide nanowires/nanorods (by partially reducing WO_3 to suboxides), stage 1, which were then sulfurized for conversion to WS_2 nanophases, stage 2.

Synthesis of W Suboxide Nanowires and Nanorods (Stage 1). This is a low-pressure CVD (LPCVD) process. The geometrical configuration of the furnace and position of boats with precursor materials are shown in Supporting Information, Figure S1. Differences in process substrate position/temperature, discussed in the main text, led to the formation of (i) long, out-of-plane nanowires, (ii) clusters of short nanorods, and (iii) in-plane nanorods of suboxides, as described below.

WO_{3-x} nanowires/nanorods were synthesized on SiO_2/Si (*i.e.*, 300 nm thermal oxide), without any catalysts. Typically, 60 mg tungsten(VI) oxide (99.998%, Alfa Aesar) and 400 mg sulfur powder (99.5%, Alfa Aesar) were used as precursors. The SiO_2/Si substrates were cleaned by sonication in acetone, isopropanol (both HPLC grade), and deionized water, in sequence, prior to loading them in the furnace. A rotary pump pumped the tube during the whole process. Only argon (flow rate 150 sccm) was used for transporting the WO_3 and sulfur vapor to the Si/SiO_2 substrates. This LPCVD stage has two distinct periods: (i) An initial period where just WO_3 is sublimed (without S vapor being introduced into the reactor), a set of typical conditions being 1030 °C, at a pressure below 10^{-1} mbar, and for 20 min; followed by (ii) a period where S is introduced and co-evaporated together with the WO_3 over 15 min, leading to partial reduction of the WO_3 vapor, and, then, its condensation on the substrate as $WO_{2.92}$ and $WO_{2.9}$ nanostructures.

We have verified in dedicated experiments that in the conditions described in (i), WO_3 is volatile during our LPCVD process. After annealing (nonhydrated) WO_3 powder for 45 min, its weight decreased by two-thirds, while the remaining powder in the furnace pocket was verified by XRD to still be entirely WO_3 (*i.e.*, did not undergo any unexpected reduction) at the end of the annealing period. No nanowires were formed on the SiO_2/Si substrates after just this process.

Synthesis of out-of-Plane WS_2 Nanotubes, Mixed 1D and 2D Phases, and 2D Nanomesh (Stage 2). This is an atmospheric pressure CVD (APCVD) process. Out-of-plane $WO_{2.92}/WO_{2.9}$ nanowires on SiO_2/Si were heated in the 850–925 °C range, under atmospheric pressure in the furnace center, whereas 400 mg of sulfur powder (99.5%, Alfa Aesar) was heated upstream (about 40 cm) at

DOI: 10.1021/acsnano.8b06515
ACS Nano 2019, 13, 3896–3909

180 °C. Argon, at a flow rate of 100 sccm, was used to transport the sulfur vapor to the nanowires on SiO_2/Si sample. The same furnace geometry as above was employed. For generating Figure 4, where the transition between nanotube and 2D nanomesh phases was monitored, identical parts of the same initial $WO_{2.92}/WO_{2.9}$ nanowire sample were reacted at 850 °C in S environment (in the conditions described above), each for an increasing amount of time (Δt) up to 3 h, to form the series described in the figure caption.

We have also verified (by a combination of SEM, TEM, and XRD) that $WO_{2.9}$ and $WO_{2.92}$ are nonvolatile in the conditions of our APCVD process by annealing the $WO_{2.92}/WO_{2.9}$ nanowires (supported by their SiO_2/Si substrate) for 1 h just in an Ar atmosphere (*i.e.*, without the presence of S) in APCVD conditions and over the same temperature range at which the various WS_2 phases were obtained (as described above).

Synthesis of in-Plane, 2D WS_2 Domains (Stage 2). As-grown $WO_{2.92}/WO_{2.9}$ short nanorods on SiO_2/Si were heated in the 850–925 °C range in the center of the furnace, under atmospheric pressure (*i.e.*, in an APCVD process), while 400 mg of sulfur powder (99.5%, Alfa Aesar) was heated upstream (about 40 cm) at 180 °C. Argon, at 100 sccm flow rate, was used to transport the sulfur vapor to the nanorods on SiO_2/Si sample. The same furnace geometry as above was employed.

Structural Characterization of Grown Nanophases and Nanostructures. *X-ray Diffraction (XRD).* WO_{3-x} nanowires/nanorods and WS_2 nanomesh as grown on their SiO_2/Si substrates were characterized by XRD performed on a BRUKER AXS D8 Advance instrument, equipped with a Vantec-1 detector, and using CuKα radiation at λ = 1.5418 Å.

High-Resolution Transmission Electron Microscopy (HRTEM) and Selected Area Electron Diffraction (SAED). Complementary HRTEM and SAED were performed on a JEOL JEM-2100Plus microscope operated at 200 kV and using a bottom-mounted CCD camera. A drop of nanowires/nanotubes/nanomesh suspension in ethanol was drop-cast onto a mesh TEM support grid.

Raman Spectroscopy. All nanostructures, as grown on their SiO_2/Si substrates—WO_{3-x} nanowires/nanorods, WS_2 nanomesh, and in-plane, WS_2 2D domains—were characterized by Raman spectroscopy performed with a Renishaw inVia Raman microscope, using 532 nm excitation laser. Samples were illuminated through a 50× objective lens (1.9 μm diameter spot size), at a laser power of 0.7 mW, while spectra were acquired with an exposure time of 1 s and using 200 accumulations.

Scanning Electron Microscopy (SEM). The nanostructured samples, as grown on the SiO_2/Si substrates, were observed using a JEOL SEM6480LV microscope in secondary electrons (SE) mode with acceleration voltages in the 5–15 kV range depending on the penetration depth needed for the various morphologies.

Linear and Nonlinear Optical Properties. *Microscopy and Normal Incidence Reflection Measurements.* An Axioplan 2 microscope (ZEISS) with a halogen lamp and a 100× microscope objective was used, measurements being performed in bright-field mode. Microscope color images were taken with an Axiocam 105 color camera, while optical spectra were taken over the 400–950 nm spectral range with an Ocean Optics QE Pro spectrometer, using an integration time of 1 s and averaging over 10 scans. The spectra were normalized with respect to the untreated silicon wafer.

Angle-Dependent Linear Optical Characterization. A Fianium SC400-2 2 W laser source with a 1064 nm output wavelength and 20 MHz repetition rate and a 5 ps pulse spliced to an in-house fabricated supercontinuum fiber[91] capable of a 450–2400 nm spectral range was used. Two uncoated Glan-Laser polarizers were used to control the power output and polarization of the incident light. The reflected light from the sample was collected *via* a 200 μm diameter SMA fiber (0.22 NA) mounted on a fiber launch stage and measured with an Ocean Optics QE Pro spectrometer over 450–950 nm, using an integration time of 300 ms and averaging over 10 scans. An automated setup was used to determine the reflected light angle. The spectra were normalized with respect to the untreated silicon wafer.

Second Harmonic Generation (SHG) Measurements. A femtosecond laser (MaiTai HP from Spectra Physics), tuned to a wavelength of 800 nm, provided the incident fundamental beam. The laser produced pulses at a repetition rate of 80 MHz, which are approximately 100 fs long in time with a bandwidth of 10 nm. Two crossed polarizers (Glan-Laser calcite antireflection coated) controlled the laser power. An achromatic half-waveplate ensured that the incident beam is P-polarized (horizontal polarization). Two colored glass bandpass filters were used to reject any spurious light at the second harmonic. An achromatic lens (focal length 150 mm, antireflection coated) focused the beam onto the sample at an incident angle of 45° relative to the sample. Another achromatic lens (focal length 150 mm, antireflection coated) collimated the SHG in reflection, while a colored bandpass filter rejected the fundamental beam, leaving only the SHG. The signal beam was focused into a cooled photomultiplier tube (PMT) using an antireflection-coated lens (focal length 200 mm). The PMT produced current pulses, which were pre-amplified and fed into a gated photon counter. The data point for each incident power was the average of 20 measurements, where the counting duration of each measurement was 5 s.

ASSOCIATED CONTENT

Supporting Information

The Supporting Information is available free of charge on the ACS Publications website at DOI: 10.1021/acsnano.8b06515.

(i) CVD setup for nanostructure synthesis, and phase diagram for WO_{3-x} phases. (ii) Characterization (XRD, SEM, and HRTEM) of grown WO_{3-x} nanowires and nanorods. (iii) Raman characterization of WS_2 nanophases. (iv) Electrical characterization of WS_2 2D nanomesh. (v) Atomistic description of layer-by-layer evolution from WO_3 to WS_2 *via* $WO_{2.92}/WO_{2.9}$ Magnéli phases (PDF)

AUTHOR INFORMATION

Corresponding Author

*E-mail: a.ilie@bath.ac.uk.

ORCID

Ventsislav Kolev Valev: 0000-0001-9951-1836

Adelina Ilie: 0000-0001-7718-1880

Author Contributions

A.I. and Z.L. designed the material growth-related program of work, while A.I. supervised the work. Z.L. performed the experiments. Z.L. and A.I. analyzed the data and co-wrote the growth part of the paper. V.K.V. and A.I. selected the optical measurements performed. V.K.V. supervised the optics-related work. A.W.A.M., C.K., and D.C.H. performed the optics experiments, and together with V.K.V. and A.I. (with contributions from Z.L.) analyzed the data and co-wrote the optics-related part of manuscript.

Notes

The authors declare no competing financial interest.

ACKNOWLEDGMENTS

Z.L. gratefully acknowledges a studentship from the University of Bath. V.K.V. acknowledges a Royal Society University Research Fellowship and Royal Society grants CHG \R1\170067, PEF1\170015, and RGF\EA\180228 as well as STFC ST/R005842/1. D.C.H. acknowledges funding and support from the Engineering and Physical Sciences Research Council, UK, *via* the Centre for Doctoral Training in Condensed Matter Physics (CDTCMP), grant no. EP/

DOI: 10.1021/acsnano.8b06515
ACS Nano 2019, 13, 3896–3909

L015544/1. We thank Kei Takashina and Alessandro Narduzzo for assistance with the electrical characterization of the 2D nanomesh and William Wadsworth and Andriy Gorbach for useful discussions on saturable absorption and cavity modes.

REFERENCES

(1) Mak, K. F.; Lee, C.; Hone, J.; Shan, J.; Heinz, T. F. Atomically Thin MoS_2: a New Direct-Gap Semiconductor. *Phys. Rev. Lett.* **2010**, *105*, 136805.
(2) Splendiani, A.; Sun, L.; Zhang, Y.; Li, T.; Kim, J.; Chim, C.-Y.; Galli, G.; Wang, F. Emerging Photoluminescence in Monolayer MoS_2. *Nano Lett.* **2010**, *10*, 1271−1275.
(3) Ramakrishna Matte, H.; Gomathi, A.; Manna, A. K.; Late, D. J.; Datta, R.; Pati, S. K.; Rao, C. MoS_2 and WS_2 Analogues of Graphene. *Angew. Chem., Int. Ed.* **2010**, *49*, 4059−4062.
(4) Ding, Y.; Wang, Y.; Ni, J.; Shi, L.; Shi, S.; Tang, W. First Principles Study of Structural, Vibrational and Electronic Properties of Graphene-Like MX_2 (M= Mo, Nb, W, Ta; X= S, Se, Te) Monolayers. *Phys. B* **2011**, *406*, 2254−2260.
(5) Wang, Q. H.; Kalantar-Zadeh, K.; Kis, A.; Coleman, J. N.; Strano, M. S. Electronics and Optoelectronics of Two-Dimensional Transition Metal Dichalcogenides. *Nat. Nanotechnol.* **2012**, *7*, 699−712.
(6) Lee, Y. H.; Zhang, X. Q.; Zhang, W.; Chang, M. T.; Lin, C. T.; Chang, K. D.; Yu, Y. C.; Wang, J. T. W.; Chang, C. S.; Li, L. J.; Lin, T.-W. Synthesis of Large-Area MoS_2 Atomic Layers with Chemical Vapor Deposition. *Adv. Mater.* **2012**, *24*, 2320−2325.
(7) Huang, J.-K.; Pu, J.; Hsu, C.-L.; Chiu, M.-H.; Juang, Z.-Y.; Chang, Y.-H.; Chang, W.-H.; Iwasa, Y.; Takenobu, T.; Li, L.-J. Large-Area Synthesis of Highly Crystalline WSe_2 Monolayers and Device Applications. *ACS Nano* **2014**, *8*, 923−930.
(8) Ling, X.; Lee, Y.-H.; Lin, Y.; Fang, W.; Yu, L.; Dresselhaus, M. S.; Kong, J. Role of the Seeding Promoter in MoS_2 Growth by Chemical Vapor Deposition. *Nano Lett.* **2014**, *14*, 464−472.
(9) Cong, C.; Shang, J.; Wu, X.; Cao, B.; Peimyoo, N.; Qiu, C.; Sun, L.; Yu, T. Synthesis and Optical Properties of Large-Area Single-Crystalline 2D Semiconductor WS_2 Monolayer from Chemical Vapor Deposition. *Adv. Opt. Mater.* **2014**, *2*, 131−136.
(10) Zhou, H.; Wang, C.; Shaw, J. C.; Cheng, R.; Chen, Y.; Huang, X.; Liu, Y.; Weiss, N. O.; Lin, Z.; Huang, Y.; Duan, X. Large Area Growth and Electrical Properties of P-Type WSe_2 Atomic Layers. *Nano Lett.* **2015**, *15*, 709−713.
(11) Wang, X.; Gong, Y.; Shi, G.; Chow, W. L.; Keyshar, K.; Ye, G.; Vajtai, R.; Lou, J.; Liu, Z.; Ringe, E.; Tay, B. K.; Ajayan, P. M. Chemical Vapor Deposition Growth of Crystalline Monolayer $MoSe_2$. *ACS Nano* **2014**, *8*, 5125−5131.
(12) Gong, Y.; Ye, G.; Lei, S.; Shi, G.; He, Y.; Lin, J.; Zhang, X.; Vajtai, R.; Pantelides, S. T.; Zhou, W.; Li, B.; Ajayan, P. M. Synthesis of Millimeter-Scale Transition Metal Dichalcogenides Single Crystals. *Adv. Funct. Mater.* **2016**, *26*, 2009−2015.
(13) Wang, S.; Pacios, M.; Bhaskaran, H.; Warner, J. H. Substrate Control for Large Area Continuous Films of Monolayer MoS_2 by Atmospheric Pressure Chemical Vapor Deposition. *Nanotechnology* **2016**, *27*, 085604.
(14) Wilson, J.; Yoffe, A. The Transition Metal Dichalcogenides Discussion and Interpretation of the Observed Optical, Electrical and Structural Properties. *Adv. Phys.* **1969**, *18*, 193−335.
(15) Zhu, Z.; Cheng, Y.; Schwingenschlögl, U. Giant Spin-Orbit-Induced Spin Splitting in Two-Dimensional Transition-Metal Dichalcogenide Semiconductors. *Phys. Rev. B: Condens. Matter Mater. Phys.* **2011**, *84*, 153402.
(16) Mao, D.; Zhang, S.; Wang, Y.; Gan, X.; Zhang, W.; Mei, T.; Wang, Y.; Wang, Y.; Zeng, H.; Zhao, J. WS_2 Saturable Absorber for Dissipative Soliton Mode Locking at 1.06 and 1.55 μm. *Opt. Express* **2015**, *23*, 27509−27519.
(17) Lin, X.; Liu, Y.; Wang, K.; Wei, C.; Zhang, W.; Yan, Y.; Li, Y. J.; Yao, J.; Zhao, Y. S. Two-Dimensional Pyramid-Like WS_2 Layered Structures for Highly Efficient Edge Second-Harmonic Generation. *ACS Nano* **2018**, *12*, 689−696.
(18) Shi, Y.; Li, H.; Li, L.-J. Recent Advances in Controlled Synthesis of Two-Dimensional Transition Metal Dichalcogenides *via* Vapour Deposition Techniques. *Chem. Soc. Rev.* **2015**, *44*, 2744−2756.
(19) Zhang, Y.; Zhang, Y.; Ji, Q.; Ju, J.; Yuan, H.; Shi, J.; Gao, T.; Ma, D.; Liu, M.; Chen, Y.; Song, X.; Hwang, H. Y.; Cui, Y.; Liu, Z. Controlled Growth of High-Quality Monolayer WS_2 Layers on Sapphire and Imaging Its Grain Boundary. *ACS Nano* **2013**, *7*, 8963−8971.
(20) Whitby, R.; Hsu, W.; Boothroyd, C.; Brigatti, K.; Kroto, H.; Walton, D. WS_2 Layer Formation on Multi-Walled Carbon Nanotubes. *Appl. Phys. A: Mater. Sci. Process.* **2003**, *76*, 527−532.
(21) Feldman, Y.; Frey, G.; Homyonfer, M.; Lyakhovitskaya, V.; Margulis, L.; Cohen, H.; Hodes, G.; Hutchison, J.; Tenne, R. Bulk Synthesis of Inorganic Fullerene-Like MS_2 (M= Mo, W) from the Respective Trioxides and the Reaction Mechanism. *J. Am. Chem. Soc.* **1996**, *118*, 5362−5367.
(22) Sloan, J.; Hutchison, J. L.; Tenne, R.; Feldman, Y.; Tsirlina, T.; Homyonfer, M. Defect and Ordered Tungsten Oxides Encapsulated inside 2H−WX_2 (X= S and Se) Fullerene-Related Structures. *J. Solid State Chem.* **1999**, *144*, 100−117.
(23) Cain, J. D.; Shi, F.; Wu, J.; Dravid, V. P. Growth Mechanism of Transition Metal Dichalcogenide Monolayers: The Role of Self-Seeding Fullerene Nuclei. *ACS Nano* **2016**, *10*, 5440−5445.
(24) Rong, Y.; Fan, Y.; Koh, A. L.; Robertson, A. W.; He, K.; Wang, S.; Tan, H.; Sinclair, R.; Warner, J. H. Controlling Sulphur Precursor Addition for Large Single Crystal Domains of WS_2. *Nanoscale* **2014**, *6*, 12096−12103.
(25) Hu, S.; Wang, X.; Meng, L.; Yan, X. Controlled Synthesis and Mechanism of Large-Area WS_2 Flakes by Low-Pressure Chemical Vapor Deposition. *J. Mater. Sci.* **2017**, *52*, 7215−7223.
(26) Elías, A. L.; Perea-López, N.; Castro-Beltrán, A.; Berkdemir, A.; Lv, R.; Feng, S.; Long, A. D.; Hayashi, T.; Kim, Y. A.; Endo, M.; Gutiérrez, H. R.; Pradhan, N. R.; Balicas, L.; Mallouk, T. E.; López-Urías, F.; Terrones, H.; Terrones, M. Controlled Synthesis and Transfer of Large-Area WS_2 Sheets: from Single Layer to Few Layers. *ACS Nano* **2013**, *7*, 5235−5242.
(27) Liu, P.; Luo, T.; Xing, J.; Xu, H.; Hao, H.; Liu, H.; Dong, J. Large-Area WS_2 Film with Big Single Domains Grown by Chemical Vapor Deposition. *Nanoscale Res. Lett.* **2017**, *12*, 558.
(28) Xie, Y.; Wang, Z.; Zhan, Y.; Zhang, P.; Wu, R.; Jiang, T.; Wu, S.; Wang, H.; Zhao, Y.; Nan, T.; Ma, X. Controllable Growth of Monolayer MoS_2 by Chemical Vapor Deposition *via* Close MoO_2 Precursor for Electrical and Optical Applications. *Nanotechnology* **2017**, *28*, 084001.
(29) Rossi, A.; Büch, H.; Di Rienzo, C.; Miseikis, V.; Convertino, D.; Al-Temimy, A.; Voliani, V.; Gemmi, M.; Piazza, V.; Coletti, C. Scalable Synthesis of WS_2 on Graphene and h-BN: an All-2D Platform for Light-Matter Transduction. *2D Mater.* **2016**, *3*, 031013.
(30) Gao, Y.; Liu, Z.; Sun, D.-M.; Huang, L.; Ma, L.-P.; Yin, L.-C.; Ma, T.; Zhang, Z.; Ma, X.-L.; Peng, L.-M.; Cheng, H.-M.; Ren, W. Large-Area Synthesis of High-Quality and Uniform Monolayer WS_2 on Reusable Au Foils. *Nat. Commun.* **2015**, *6*, 8569.
(31) Wu, D.; Min, T.; Zhou, J.; Li, C.; Ma, G.; Lu, G.; Xia, M.; Gu, Z. Effect of Substrate Symmetry on the Dendrite Morphology of MoS_2 Film Synthesized by CVD. *Sci. Rep.* **2017**, *7*, 15166.
(32) Chen, J.; Liu, B.; Liu, Y.; Tang, W.; Nai, C. T.; Li, L.; Zheng, J.; Gao, L.; Zheng, Y.; Shin, H. S.; Jeong, H. Y.; Loh, K. P. Chemical Vapor Deposition of Large-Sized Hexagonal WSe_2 Crystals on Dielectric Substrates. *Adv. Mater.* **2015**, *27*, 6722−6727.
(33) Özden, A.; Şar, H.; Yeltik, A.; Madenoğlu, B.; Sevik, C.; Ay, F.; Perkgöz, N. K. CVD Grown 2D MoS_2 Layers: a Photoluminescence and Fluorescence Lifetime Imaging Study. *Phys. Status Solidi RRL* **2016**, *10*, 792−796.
(34) Özden, A.; Ay, F.; Sevik, C.; Perkgöz, N. K. CVD Growth of Monolayer MoS_2: Role of Growth Zone Configuration and Precursors Ratio. *Jpn. J. Appl. Phys.* **2017**, *56*, 06GG05.

DOI: 10.1021/acsnano.8b06515
ACS Nano 2019, 13, 3896−3909

(35) Rothschild, A.; Sloan, J.; Tenne, R. Growth of WS_2 Nanotubes Phases. *J. Am. Chem. Soc.* **2000**, *122*, 5169−5179.
(36) Zak, A.; Sallacan-Ecker, L.; Margolin, A.; Feldman, Y.; Popovitz-Biro, R.; Albu-Yaron, A.; Genut, M.; Tenne, R. Scaling up of the WS_2 Nanotubes Synthesis. *Fullerenes, Nanotubes, Carbon Nanostruct.* **2010**, *19*, 18−26.
(37) Lee, Y.-H.; Yu, L.; Wang, H.; Fang, W.; Ling, X.; Shi, Y.; Lin, C.-T.; Huang, J.-K.; Chang, M.-T.; Chang, C.-S.; Dresselhaus, M.; Palacios, T.; Li, L.-J.; Kong, J. Synthesis and Transfer of Single-Layer Transition Metal Disulfides on Diverse Surfaces. *Nano Lett.* **2013**, *13*, 1852−1857.
(38) Füchtbauer, H. G.; Tuxen, A. K.; Moses, P. G.; Topsøe, H.; Besenbacher, F.; Lauritsen, J. V. Morphology and Atomic-Scale Structure of Single-Layer WS_2 Nanoclusters. *Phys. Chem. Chem. Phys.* **2013**, *15*, 15971−15980.
(39) Li, X. L.; Li, Y. D. Formation of MoS_2 Inorganic Fullerenes (IFs) by the Reaction of MoO_3 Nanobelts and S. *Chem. - Eur. J.* **2003**, *9*, 2726−2731.
(40) Ji, Q.; Zhang, Y.; Zhang, Y.; Liu, Z. Chemical Vapour Deposition of Group-VIb Metal Dichalcogenide Monolayers: Engineered Substrates from Amorphous to Single Crystalline. *Chem. Soc. Rev.* **2015**, *44*, 2587−2602.
(41) Wang, S.; Rong, Y.; Fan, Y.; Pacios, M.; Bhaskaran, H.; He, K.; Warner, J. H. Shape Evolution of Monolayer MoS_2 Crystals Grown by Chemical Vapor Deposition. *Chem. Mater.* **2014**, *26*, 6371−6379.
(42) Yang, P.; Zou, X.; Zhang, Z.; Hong, M.; Shi, J.; Chen, S.; Shu, J.; Zhao, L.; Jiang, S.; Zhou, X.; Huan, Y.; Xie, C.; Gao, P.; Chen, Q.; Zhang, Q.; Liu, Z.; Zhang, Y. Batch Production of 6-Inch Uniform Monolayer Molybdenum Disulfide Catalyzed by Sodium in Glass. *Nat. Commun.* **2018**, *9*, 979.
(43) Fu, Q.; Wang, W.; Yang, L.; Huang, J.; Zhang, J.; Xiang, B. Controllable Synthesis of High Quality Monolayer WS_2 on a SiO_2/Si Substrate by Chemical Vapor Deposition. *RSC Adv.* **2015**, *5*, 15795−15799.
(44) Ling, M.; Blackman, C. Growth Mechanism of Planar or Nanorod Structured Tungsten Oxide Thin Films Deposited *via* Aerosol Assisted Chemical Vapour Deposition (AACVD). *Phys. Status Solidi C* **2015**, *12*, 869−877.
(45) Shen, Z.; Zhao, Z.; Qian, J.; Peng, Z.; Fu, X. Synthesis of WO_3−X Nanomaterials with Controlled Morphology and Composition for Highly Efficient Photocatalysis. *J. Mater. Res.* **2016**, *31*, 1065−1076.
(46) Rieck, G. D. *Tungsten and Its Compounds*, 1st ed.; Pergamon: Oxford, U.K., 1967; pp 68−113.
(47) Garcia-Sanchez, R. F.; Ahmido, T.; Casimir, D.; Baliga, S.; Misra, P. Thermal Effects Associated with the Raman Spectroscopy of WO_3 Gas-Sensor Materials. *J. Phys. Chem. A* **2013**, *117*, 13825−13831.
(48) Wang, X. H.; Zheng, C. C.; Ning, J. Q. Influence of Curvature Strain and Van Der Waals Force on the Inter-Layer Vibration Mode of WS_2 Nanotubes: a Confocal Micro-Raman Spectroscopic Study. *Sci. Rep.* **2016**, *6*, 33091.
(49) Polyakov, B.; Kuzmin, A.; Smits, K.; Zideluns, J.; Butanovs, E.; Butikova, J.; Vlassov, S.; Piskunov, S.; Zhukovskii, Y. F. Unexpected Epitaxial Growth of a Few WS_2 Layers on $\{1\bar{1}00\}$ Facets of ZnO Nanowires. *J. Phys. Chem. C* **2016**, *120*, 21451−21459.
(50) Feldman, Y.; Wasserman, E.; Srolovitz, D.; Tenne, R. High-Rate, Gas-Phase Growth of MoS_2 Nested Inorganic Fullerenes and Nanotubes. *Science* **1995**, *267*, 222−225.
(51) Polyakov, A. Y.; Zak, A.; Tenne, R.; Goodilin, E. A.; Solntsev, K. A. Nanocomposites Based on Tubular and Onion Nanostructures of Molybdenum and Tungsten Disulfides: Inorganic Design, Functional Properties and Applications. *Russ. Chem. Rev.* **2018**, *87*, 251.
(52) Qian, J.; Zhao, Z.; Shen, Z.; Zhang, G.; Peng, Z.; Fu, X. Oxide Vacancies Enhanced Visible Active Photocatalytic $W_{19}O_{55}$ NMRS *via* Strong Adsorption. *RSC Adv.* **2016**, *6*, 8061−8069.
(53) Chen, Y.; Li, Y.; Wang, Y.; Tian, T.; Qin, L.-C. Thin WS_2 Nanotubes from $W_{18}O_{49}$ Nanowires. *Mater. Res. Lett.* **2017**, *5*, 508−515.
(54) Zeng, Z.; Yin, Z.; Huang, X.; Li, H.; He, Q.; Lu, G.; Boey, F.; Zhang, H. Single-Layer Semiconducting Nanosheets: High-Yield Preparation and Device Fabrication. *Angew. Chem., Int. Ed.* **2011**, *50*, 11093−11097.
(55) Nethravathi, C.; Jeffery, A. A.; Rajamathi, M.; Kawamoto, N.; Tenne, R.; Golberg, D.; Bando, Y. Chemical Unzipping of WS_2 Nanotubes. *ACS Nano* **2013**, *7*, 7311−7317.
(56) Huo, N.; Yue, Q.; Yang, J.; Yang, S.; Li, J. Abnormal Photocurrent Response and Enhanced Photocatalytic Activity Induced by Charge Transfer between WS_2 Nanosheets and WO_3 Nanoparticles. *ChemPhysChem* **2013**, *14*, 4069−4073.
(57) Asres, G. A.; Dombovari, A.; Sipola, T.; Puskás, R.; Kukovecz, A.; Kónya, Z.; Popov, A.; Lin, J.-F.; Lorite, G. S.; Mohl, M.; Toth, G.; Spetz, A. L.; Kordas, K. A Novel WS_2 Nanowire-Nanoflake Hybrid Material Synthesized from WO_3 Nanowires in Sulfur Vapor. *Sci. Rep.* **2016**, *6*, 25610.
(58) Najmaei, S.; Liu, Z.; Zhou, W.; Zou, X.; Shi, G.; Lei, S.; Yakobson, B. I.; Idrobo, J.-C.; Ajayan, P. M.; Lou, J. Vapour Phase Growth and Grain Boundary Structure of Molybdenum Disulphide Atomic Layers. *Nat. Mater.* **2013**, *12*, 754.
(59) Kumar, P.; Balakrishnan, V. Growth and Microstructural Evolution of WS_2 Nanostructures with Tunable Field and Light Modulated Electrical Transport. *Appl. Surf. Sci.* **2018**, *436*, 846−853.
(60) Kumar, P.; Balakrishnan, V. Nanosculpting of Atomically Thin 2D Materials for Site-Specific Photoluminescence Modulation. *Adv. Opt. Mater.* **2018**, *6*, 1701284.
(61) Lin, Y.-C.; Zhang, W.; Huang, J.-K.; Liu, K.-K.; Lee, Y.-H.; Liang, C.-T.; Chu, C.-W.; Li, L.-J. Wafer-Scale MoS_2 Thin Layers Prepared by MoO_3 Sulfurization. *Nanoscale* **2012**, *4*, 6637−6641.
(62) Wu, S.; Huang, C.; Aivazian, G.; Ross, J. S.; Cobden, D. H.; Xu, X. Vapor−Solid Growth of High Optical Quality MoS_2 Monolayers with Near-Unity Valley Polarization. *ACS Nano* **2013**, *7*, 2768−2772.
(63) Xu, Z.-Q.; Zhang, Y.; Lin, S.; Zheng, C.; Zhong, Y. L.; Xia, X.; Li, Z.; Sophia, P. J.; Fuhrer, M. S.; Cheng, Y.-B.; Bao, Q. Synthesis and Transfer of Large-Area Monolayer WS_2 Crystals: Moving Toward the Recyclable Use of Sapphire Substrates. *ACS Nano* **2015**, *9*, 6178−6187.
(64) Gabai, R.; Ismach, A.; Joselevich, E. Nanofacet Lithography: a New Bottom-up Approach to Nanopatterning and Nanofabrication by Soft Replication of Spontaneously Faceted Crystal Surfaces. *Adv. Mater.* **2007**, *19*, 1325−1330.
(65) Nikoobakht, B. Toward Industrial-Scale Fabrication of Nanowire-Based Devices. *Chem. Mater.* **2007**, *19*, 5279−5284.
(66) Fortuna, S. A.; Wen, J.; Chun, I. S.; Li, X. Planar GaAs Nanowires on GaAs (100) Substrates: Self-Aligned, Nearly Twin-Defect Free, and Transfer-Printable. *Nano Lett.* **2008**, *8*, 4421−4427.
(67) Tsivion, D.; Schvartzman, M.; Popovitz-Biro, R.; von Huth, P.; Joselevich, E. Guided Growth of Millimeter-Long Horizontal Nanowires with Controlled Orientations. *Science* **2011**, *333*, 1003−1007.
(68) Gillet, M.; Delamare, R.; Gillet, E. Growth of Epitaxial Tungsten Oxide Nanorods. *J. Cryst. Growth* **2005**, *279*, 93−99.
(69) Zhu, D.; Shu, H.; Jiang, F.; Lv, D.; Asokan, V.; Omar, O.; Yuan, J.; Zhang, Z.; Jin, C. Capture the Growth Kinetics of CVD Growth of Two-Dimensional MoS_2. *npj 2D Mater. Appl.* **2017**, *1*, 8.
(70) Zhou, D.; Shu, H.; Hu, C.; Jiang, L.; Liang, P.; Chen, X. Unveiling the Growth Mechanism of MoS_2 with Chemical Vapor Deposition: From Two-Dimensional Planar Nucleation to Self-Seeding Nucleation. *Cryst. Growth Des.* **2018**, *18*, 1012−1019.
(71) Feldman, Y.; Lyakhovitskaya, V.; Tenne, R. Kinetics of Nested Inorganic Fullerene-Like Nanoparticle Formation. *J. Am. Chem. Soc.* **1998**, *120*, 4176−4183.
(72) Li, S.; Wang, S.; Tang, D.-M.; Zhao, W.; Xu, H.; Chu, L.; Bando, Y.; Golberg, D.; Eda, G. Halide-Assisted Atmospheric Pressure Growth of Large WSe_2 and WS_2 Monolayer Crystals. *Appl. Mater. Today* **2015**, *1*, 60−66.
(73) Zhao, W.; Ghorannevis, Z.; Chu, L.; Toh, M.; Kloc, C.; Tan, P.-H.; Eda, G. Evolution of Electronic Structure in Atomically Thin Sheets of WS_2 and WSe_2. *ACS Nano* **2013**, *7*, 791−797.

DOI: 10.1021/acsnano.8b06515
ACS Nano 2019, 13, 3896−3909

(74) Yadgarov, L.; Višić, B.; Abir, T.; Tenne, R.; Polyakov, A. Y.; Levi, R.; Dolgova, T. V.; Zubyuk, V. V.; Fedyanin, A. A.; Goodilin, E. A.; Ellenbogen, T.; Tenne, R.; Oron, D. Strong Light–Matter Interaction in Tungsten Disulfide Nanotubes. *Phys. Chem. Chem. Phys.* **2018**, *20*, 20812–20820.
(75) Madhavi, V.; Kondaiah, P.; Hussain, O. M.; Uthanna, S. Structural, Optical, and Luminescence Properties of Reactive Magnetron Sputtered Tungsten Oxide Thin Films. *ISRN Opt.* **2012**, *2012*, 801468.
(76) Wang, K.; Wang, J.; Fan, J.; Lotya, M.; O'Neill, A.; Fox, D.; Feng, Y.; Zhang, X.; Jiang, B.; Zhao, Q.; Zhang, H.; Coleman, J. N.; Zhang, L.; Blau, W. J. Ultrafast Saturable Absorption of Two-Dimensional MoS_2 Nanosheets. *ACS Nano* **2013**, *7*, 9260–9267.
(77) Fu, X.; Qian, J.; Qiao, X.; Tan, P.; Peng, Z. Nonlinear Saturable Absorption of Vertically Stood WS_2 Nanoplates. *Opt. Lett.* **2014**, *39*, 6450–6453.
(78) Mao, D.; Zhang, S.; Wang, Y.; Gan, X.; Zhang, W.; Mei, T.; Wang, Y.; Wang, Y.; Zeng, H.; Zhao, J. WS_2 Saturable Absorber for Dissipative Soliton Mode Locking at 1.06 and 1.55 μm. *Opt. Express* **2015**, *23*, 27509–27519.
(79) Fan, X.; Jiang, Y.; Zhuang, X.; Liu, H.; Xu, T.; Zheng, W.; Fan, P.; Li, H.; Wu, X.; Zhu, X.; Zhang, Q.; Zhou, H.; Hu, W.; Wang, X.; Sun, L.; Duan, X.; Pan, A. Broken Symmetry Induced Strong Nonlinear Optical Effects in Spiral WS_2 Nanosheets. *ACS Nano* **2017**, *11*, 4892–4898.
(80) Lee, C. H.; Chang, R. K.; Bloembergen, N. Nonlinear Electroreflectance in Silicon and Silver. *Phys. Rev. Lett.* **1967**, *18*, 167–170.
(81) Kirilyuk, A.; Rasing, T. Magnetization-Induced-Second-Harmonic Generation from Surfaces and Interfaces. *J. Opt. Soc. Am. B* **2005**, *22*, 148–167.
(82) Jeong, J.-W.; Shin, S.-C.; Dadoenkova, N. N.; Lyubchanskii, I. L.; Valev, V. K.; Rasing, T. Direct Observation of Controlled Strain-Induced Second Harmonic Generation in a $Co_{0.25}Pd_{0.75}$ Thin Film on a $Pb(ZrTi)O_3$ Substrate. *Appl. Phys. Lett.* **2007**, *90*, 044108.
(83) Collins, J. T.; Rusimova, K. R.; Hooper, D. C.; Jeong, H. H.; Ohnoutek, L.; Pradaux-Caggiano, F.; Verbiest, T.; Carbery, D. R.; Fischer, P.; Valev, V. K. First Observation of Optical Activity in Hyper-Rayleigh Scattering. *Phys. Rev. X* **2019**, *9*, 011024.
(84) Hooper, D. C.; Kuppe, C.; Wang, D.; Wang, W.; Guan, J.; Odom, T. W.; Valev, V. K. Second Harmonic Spectroscopy of Surface Lattice Resonances. *Nano Lett.* **2019**, *19*, 165–172.
(85) Valev, V. K.; Kirilyuk, A.; Dalla Longa, F.; Kohlhepp, J. T.; Koopmans, B.; Rasing, T. Observation of Periodic Oscillations in Magnetization-Induced Second Harmonic Generation at the Mn/Co Interface. *Phys. Rev. B: Condens. Matter Mater. Phys.* **2007**, *75*, 012401.
(86) Bloembergen, N.; Chang, R. K.; Jha, S. S.; Lee, C. H. Optical Second-Harmonic Generation in Reflection from Media with Inversion Symmetry. *Phys. Rev.* **1968**, *174*, 813–822.
(87) Litwin, J. A.; Sipe, J. E.; van Driel, H. M. Picosecond and Nanosecond Laser-Induced Second-Harmonic Generation from Centrosymmetric Semiconductors. *Phys. Rev. B: Condens. Matter Mater. Phys.* **1985**, *31*, 5543–5546.
(88) Li, Y.; Rao, Y.; Mak, K. F.; You, Y.; Wang, S.; Dean, C. R.; Heinz, T. F. Probing Symmetry Properties of Few-Layer MoS_2 and h-BN by Optical Second-Harmonic Generation. *Nano Lett.* **2013**, *13*, 3329–3333.
(89) Janisch, C.; Wang, Y.; Ma, D.; Mehta, N.; Elías, A. L.; Perea-López, N.; Terrones, M.; Crespi, V.; Liu, Z. Extraordinary Second Harmonic Generation in Tungsten Disulfide Monolayers. *Sci. Rep.* **2015**, *4*, 5530.
(90) Woodward, R.; Kelleher, E.; Howe, R.; Hu, G.; Torrisi, F.; Hasan, T.; Popov, S.; Taylor, J. Tunable Q-Switched Fiber Laser Based on Saturable Edge-State Absorption in Few-Layer Molybdenum Disulfide (MoS_2). *Opt. Express* **2014**, *22*, 31113–31122.
(91) Stone, J. M.; Knight, J. C. Visibly "White" Light Generation in Uniform Photonic Crystal Fiber Using a Microchip Laser. *Opt. Express* **2008**, *16*, 2670–2675.

DOI: 10.1021/acsnano.8b06515
ACS Nano 2019, 13, 3896–3909